Int J Fract (2010) 163:67–83
DOI 10.1007/s10704-010-9473-x

ORIGINAL PAPER

Comparison of fully coupled modeling and experiments for electromagnetic forming processes in finitely strained solids

J. D. Thomas · N. Triantafyllidis · A. Vivek · G. S. Daehn · J. R. Bradley

Received: 26 August 2009 / Accepted: 25 February 2010 / Published online: 2 April 2010

Abstract In fracture and fragmentation research the technique of electromagnetic forming, which uses electromagnetic (Lorentz) body forces to shape metallic parts, is finding significant use due to the high velocity, high strain rate loading it can impart without contact on workpieces. The same process is also becoming increasingly relevant for manufacturing processes in sheet metal forming, where this technique offers several advantages: speed, repeatability, non-contact loading, reduced springback and considerable ductility increase in several metals. Current modeling techniques for these coupled electromagnetic and thermomechanical processes are not based on coupled variational principles that can simultaneously account for electromagnetic and mechanical effects. Typically, separate solutions to the electromagnetic (Maxwell) and motion (Newton) equations are combined in staggered or lock-step methods, sequentially solving the mechanical and electromagnetic problems. To address this issue, Thomas and Triantafyllidis (J Mech Phys Solids 57:1391–1416, 2009) have recently introduced a fully coupled Lagrangian (reference configuration) variational principle, involving the magnetic field potential and the displacement field as independent variables. The corresponding Euler-Lagrange equations are Maxwell's and Newton's equations in the reference configuration under the eddy current approximation. This novel approach is used here to simulate free expansion experiments of AA6063-T6 aluminum tubes. A viscoplastic constitutive model, developed independently by the authors (Thomas et al. Acta Mater 55:2863–2873, 2007) for necking experiments in tubes of the same aluminum alloy, is used in the simulations. The measured electric currents and tube deformation—the latter obtained by Photon Doppler Velocimetry—show reasonably good agreement with the corresponding simulations, which are obtained using a variational integration numerical scheme that results in an efficient staggered solution algorithm.

Sandia is a multiprogram laboratory operated by Sandia Corporation, a Lockheed Martin Company, for the United States Department of Energy's National Nuclear Security Administration under Contract DE-AC04-94-AL85000.

J. D. Thomas (✉)
Sandia National Laboratories, Albuquerque, NM 87185, USA
e-mail: jdthom@sandia.gov

N. Triantafyllidis
Solid Mechanics Laboratory & Department of Mechanics, Ecole Polytechnique, Palaiseau 91128, France

N. Triantafyllidis
Aerospace Engineering Department, The University of Michigan, Ann Arbor, MI 48109, USA

A. Vivek · G. S. Daehn
Materials Science and Engineering Department, The Ohio State University, Columbus, OH 43210, USA

J. R. Bradley
Materials and Processes Laboratory, General Motors R&D Center, Warren, MI 48090, USA

Keywords Electromagnetics · Continuum mechanics · Variational principles · Multiphysics · Experimental techniques

1 Introduction

Recent work on dynamic fracture and fragmentation, and on industrial manufacturing processes for products such as fuel cell plates, has renewed interest in the high velocity technique of electromagnetic forming (EMF). A typical EMF set-up consists of a large capacitor bank connected in series with a forming coil (often a copper wire solenoid). The capacitor bank is discharged through the coil to produce a large transient current, which induces electric currents in the nearby metallic workpiece. Lorentz forces result and cause workpiece deformation over a characteristic process time on the order of 50 μs. The EMF process has many desirable characteristics, including precise control of the input electric energy, which makes the process repeatable, and non-contact loading, which allows the use of single side tooling, an advantage in the forming of parts that are already coated on one side. In addition, the interest of EMF for industrial applications is due to the observed springback reduction and a significant increase in workpiece ductility over conventional forming techniques (Balanethiram and Daehn 1992, 1994; Imbert et al. 2005a,b; Seth and Daehn 2005; Seth et al. 2005), though the mechanism behind this ductility increase is still being debated (Thomas et al. 2007; Thomas and Triantafyllidis 2007; Zhang et al. 2008; Zhang and Ravi-Chandar 2006, 2008). Of particular interest to the present work is the study of time–dependent deformations and electric currents in solids induced by electromagnetic loading processes.

The body of experimental work in the literature on high strain rate metal forming, and on EMF in particular, is extensive. Representative examples may be found in Imbert et al. (2005a,b), Oliveira and Worswick (2003), Oliveira et al. (2005), Seth et al. (2005), where the onset of localization and failure in thin sheets formed with EMF is discussed. Hu and Daehn (1996), Seth and Daehn (2005), Zhang et al. (2008), Zhang and Ravi-Chandar (2006, 2008) present similar work with EMF tube and ring expansion. Moreover, numerous EMF design studies have been carried out (e.g. Kamal and Daehn 2007; Park et al. 2004). Primarily these as well as similar works in the corresponding literature are interested in the mechanical effects of EMF such as localization, failure by fragmentation or formability. To a lesser extent experiments on EMF address the aspects of interest to the present work, i.e. the time dependent deformation and electric currents induced by EMF.

On the theoretical side, coupled electromagnetic-mechanical processes have thus far typically been modeled through the use of separate electromagnetic and mechanical solvers, combined either loosely or in more tightly coupled staggered approaches. Some example works that employ commercial finite element method codes are Karch and Roll (2005), L'Eplattenier et al. (2006), Oliveira et al. (2005). In addition, El-Azab et al. (2003), Kleiner et al. (2004), Svendsen and Chanda (2005) review coupled techniques for EMF solutions, and Stiemer et al. (2006) introduce a finite element methodology specific to electromagnetic-mechanical problems (see also Reese et al. 2005; Svendsen and Chanda 2005; Unger et al. 2006). There is further work specific to electromagnetic-mechanical problems using the Arbitrary Lagrangian-Eulerian (ALE) framework by Fenton and Daehn (1998), Rieben et al. (2006), Stiemer et al. (2007), Unger et al. (2008). However, despite the sophistication of the above mentioned works, all are based on separate solutions of the electromagnetic and mechanical boundary value problems and do not make use of a unified electromagnetic/mechanical variational formulation.

The present work's goal is to employ a recently proposed (Thomas and Triantafyllidis 2009), variationally based, fully coupled model of electromagnetic-mechanical processes, which has been specifically developed in the context of EMF, to simulate a set of free expansion experiments for AA6063-T6 aluminum tubes. In Sect. 2 we present the variational principle introduced by Thomas and Triantafyllidis (2009) for electromagnetic–mechanical problems under the eddy current approximation and continue with the description of the material constitutive response. The restriction to axisymmetric forming, as well as the special considerations needed for the forming coil simulation, conclude the problem formulation. The numerical solution algorithm, which is derived using a variational integration technique based on the previously introduced coupled variational principle, is outlined in Sect. 3. Section 4 discusses the experimental set-up, procedure and data measurement techniques used to measure the time varying electric currents and mid-section tube displacements, the latter obtained by Photon Doppler

Velocimetry. In Sect. 5, results of the tube expansion experiments and simulations are presented and compared. The work ends with the concluding remarks in Sect. 6.

2 Problem formulation

The formulation employed in the present work to model coupled electromagnetic-mechanical processes is based on a variational principle in the reference configuration (Lax and Nelson 1976; Maugin 1988; Trimarco 2007; Trimarco and Maugin 2001) which has recently been adapted for the EMF processes of interest, using the eddy current approximation, by Thomas and Triantafyllidis (2009). The resulting Euler-Lagrange equations in the reference configuration agree with those derived from a direct approach (Kovetz 2000; Lax and Nelson 1976; Thomas and Triantafyllidis 2009).

This section begins with a development of the variational formulation in the reference configuration under the eddy current assumption. It continues with a presentation of the electromagnetic and mechanical constitutive responses employed, and since the experiments of interest may be modeled as cases of axisymmetric forming, this section concludes with the restriction of the general theory to axisymmetry. For additional details of the formulation the interested reader may consult Thomas and Triantafyllidis (2009).

2.1 Variational formulation in 3-D

The present work begins with the reference configuration variational formulation under the eddy current approximation, assuming no magnetization or polarization and only volumetric electric currents and charges. The aspects typical of EMF processes that justify the eddy current approximation: the material velocities are much less than the speed of light, the effective electric current frequencies are on the order of 10 kHz, the geometry is on the order of 1 mm and the material electrical conductivities are large. The eddy current approximation essentially consists of neglecting the energy of the electric fields and implies displacement currents are neglected, which means volumetric charges are not accounted for and charge conservation must be imposed separate from the variational principle.

A reference configuration electromagnetic-mechanical Lagrangian under the eddy current approximation $\mathscr{L}$ may be written in terms of the kinetic energy $\mathscr{K}$ and potential energy $\mathscr{P}$ as:[1]

$$\mathscr{L}(\boldsymbol{A}, \dot{\boldsymbol{u}}) \equiv \mathscr{K}(\dot{\boldsymbol{u}}) - \mathscr{P}(\boldsymbol{A}, \boldsymbol{u}), \tag{2.1}$$

where $\mathscr{K}(\dot{\boldsymbol{u}})$ and $\mathscr{P}(\boldsymbol{A}, \boldsymbol{u})$ are given by:

$$\mathscr{K}(\dot{\boldsymbol{u}}) \equiv \int_{\Omega} \frac{\rho_0}{2} \left(\dot{\boldsymbol{u}} \bullet \dot{\boldsymbol{u}}\right) \, \mathrm{d}V \tag{2.2}$$

$$\mathscr{P}(\boldsymbol{A}, \boldsymbol{u}) \equiv \int_{\mathbb{R}^3} \left(\frac{1}{2\mu_0 J} (\boldsymbol{B} \bullet \boldsymbol{C} \bullet \boldsymbol{B}) - \boldsymbol{J} \bullet \boldsymbol{A} + \rho_0 (\psi - \boldsymbol{f} \bullet \boldsymbol{u}) \right) \mathrm{d}V - \int_{\partial\Omega} \boldsymbol{T} \bullet \boldsymbol{u} \, \mathrm{d}S.$$

Here the scalar field J is the determinant of the deformation gradient $\boldsymbol{F}$, $\boldsymbol{C}$ is the right Cauchy-Green tensor and $\boldsymbol{u}$ is the displacement, namely:

$$\boldsymbol{C} \equiv \boldsymbol{F}^T \bullet \boldsymbol{F}, \quad J \equiv \det(\boldsymbol{F}), \quad \boldsymbol{F} \equiv \boldsymbol{I} + \boldsymbol{u}\nabla. \tag{2.3}$$

In addition, $\boldsymbol{A}$ is a reference configuration vector potential of the corresponding magnetic field $\boldsymbol{B}$ (to be discussed subsequently), ρ_0 is the reference configuration mass density (non-zero only in the material domain Ω), μ_0 is the permeability of free space (the permeability is assumed constant throughout the problem domain), vector field $\boldsymbol{J}$ is the reference configuration conduction current density, ψ is the free energy (which here depends on $\boldsymbol{u}$ and internal variables but in the absence of magnetization and polarization does not depend on $\boldsymbol{A}$), $\boldsymbol{f}$ is the mechanical body force and $\boldsymbol{T}$ is the reference configuration mechanical surface traction. A dot superimposed on any field quantity $\dot{(\,)}$ indicates the corresponding material time derivative.

To write this Lagrangian we have used a potential formulation that identically satisfies two of the four Maxwell's equations, namely Faraday's equation and the statement of no magnetic charges. Thus, for the magnetic field we define a reference configuration vector potential $\boldsymbol{A}$ and for the electric field we define a reference configuration scalar potential Φ such that:

$$\boldsymbol{B} = \nabla \times \boldsymbol{A}, \quad \boldsymbol{E} = -\nabla\Phi - \dot{\boldsymbol{A}}, \tag{2.4}$$

where $\boldsymbol{E}$ is the reference configuration electromotive intensity and ∇ is the gradient operator in the reference

[1] Dyadic notation is employed with bold face letters denoting vectors or tensors, $\bullet$ denoting tensor contraction, and $\times$ denoting the vector product.

configuration. Notice that $\boldsymbol{E}$ does not appear explicitly in $\mathscr{L}$, and thus $\mathscr{L}$ does not depend directly on Φ. The dependence occurs indirectly through the constitutive equation for $\boldsymbol{J}$ so that Φ is not an independent field of the variational principle. Also, in this formulation $\boldsymbol{A}$ and Φ are not unique for a given $\boldsymbol{B}$ and $\boldsymbol{E}$. Thus in addition to Maxwell's and Newton's equations, a gauge condition must be satisfied for a unique solution.

Hamilton's principle states that the action integral $\mathscr{F}$, defined as the integral of the Lagrangian introduced in Eq. (2.1) over the time interval $[t_1, t_2]$, is stationary:[2]

$$\delta\mathscr{F} = 0, \quad \mathscr{F} \equiv \int_{t_1}^{t_2} \mathscr{L}\, \mathrm{d}t, \tag{2.5}$$

where $\delta\boldsymbol{A} = \boldsymbol{0}$ and $\delta\boldsymbol{u} = \boldsymbol{0}$ at $t = t_1$ and $t = t_2$. The resulting Euler-Lagrange equations are the governing equations of the electromagnetic-mechanical system.

More specifically, taking the variation of $\mathscr{F}$ with respect to $\boldsymbol{A}$ gives:

$$\begin{aligned}\mathscr{F}_{,\boldsymbol{A}}[\delta\boldsymbol{A}] &= \int_{t_1}^{t_2} \left\{ \int_{\mathbb{R}^3} \left(-\nabla\times\left(\frac{1}{\mu_0 J}\,(\boldsymbol{B}\bullet\boldsymbol{C})\right) + \boldsymbol{J}\right)\bullet\delta\boldsymbol{A}\,\mathrm{d}V \right. \\ &\quad \left. - \int_{\partial\Omega} \left[\!\!\left[\left(\boldsymbol{N}\times\left(\frac{1}{\mu_0 J}\,(\boldsymbol{B}\bullet\boldsymbol{C})\right)\right)\bullet\delta\boldsymbol{A}\right]\!\!\right] \mathrm{d}S \right\} \mathrm{d}t = 0,\end{aligned} \tag{2.6}$$

where the double bars indicate the jump in a quantity across the surface of integration with normal $\boldsymbol{N}$. The terms in parentheses in Eq. (2.6) are the reference configuration H field, $\boldsymbol{H}$, i.e.

$$\boldsymbol{H} = \frac{1}{\mu_0 J}\,(\boldsymbol{B}\bullet\boldsymbol{C})\,. \tag{2.7}$$

Thus the variation with respect to $\boldsymbol{A}$ results in the reference configuration Ampere's equation and interface condition, under the eddy current simplification, given by:[3]

$$\nabla\times\boldsymbol{H} = \boldsymbol{J}, \quad \boldsymbol{N}\times[\![\,\boldsymbol{H}\,]\!] = \boldsymbol{0}. \tag{2.8}$$

[2] Here and subsequently δ denotes the variation of a functional.

[3] By the definitions of $\boldsymbol{N}$ and the component of $\boldsymbol{A}$ tangent to the interface surface, $\boldsymbol{A}_t$, one has $[\![\,(\boldsymbol{N}\times\boldsymbol{H})\bullet\delta\boldsymbol{A}\,]\!] = (\boldsymbol{N}\times[\![\,\boldsymbol{H}\,]\!])\bullet\delta\boldsymbol{A}_t$.

Taking the variation of $\mathscr{F}$ with respect to $\boldsymbol{u}$, one has:

$$\begin{aligned}\mathscr{F}_{,\boldsymbol{u}}[\delta\boldsymbol{u}] = \int_{t_1}^{t_2} \left\{ \int_{\Omega} \left(\nabla\bullet\boldsymbol{\Pi} - \rho_0\ddot{\boldsymbol{u}} + \rho_0\boldsymbol{f}\right)\bullet\delta\boldsymbol{u}\,\mathrm{d}V \right. \\ \left. - \int_{\partial\Omega} (\boldsymbol{N}\bullet[\![\,\boldsymbol{\Pi}\,]\!] - \boldsymbol{T})\bullet\delta\boldsymbol{u}\,\mathrm{d}S \right\} \mathrm{d}t = 0,\end{aligned} \tag{2.9}$$

where $\boldsymbol{\Pi}$, the electromagnetic-mechanical first Piola-Kirchhoff stress under the eddy current approximation, is found to be:

$$\begin{aligned}\boldsymbol{\Pi} &= \boldsymbol{\Pi}_m + \boldsymbol{\Pi}_M; \\ \boldsymbol{\Pi}_m &\equiv \rho_0\left(\frac{\partial\psi}{\partial\boldsymbol{F}}\right)^T, \\ \boldsymbol{\Pi}_M &\equiv \frac{1}{\mu_0 J}\left(\boldsymbol{B}\boldsymbol{B}\bullet\boldsymbol{F}^T - \frac{1}{2}\,(\boldsymbol{B}\bullet\boldsymbol{C}\bullet\boldsymbol{B})\,\boldsymbol{F}^{-1}\right).\end{aligned} \tag{2.10}$$

The total electromagnetic-mechanical first Piola-Kirchhoff stress measure consists of two parts: $\boldsymbol{\Pi}_m$ and $\boldsymbol{\Pi}_M$, respectively the mechanical part and Maxwell (electromagnetic) part of $\boldsymbol{\Pi}$. Equation (2.9) implies the pointwise equation of motion and interface condition in the reference configuration:

$$\nabla\bullet\boldsymbol{\Pi} + \rho_0\boldsymbol{f} = \rho_0\ddot{\boldsymbol{u}}, \quad \boldsymbol{N}\bullet[\![\,\boldsymbol{\Pi}\,]\!] = \boldsymbol{T}, \tag{2.11}$$

which agrees with the electromagnetic-mechanical equation of motion derived from the direct approach when the electric displacement is neglected.

To complete the formulation, charge conservation must be imposed separately, since it cannot follow from Hamilton's principle with the eddy current simplification. The reference configuration charge conservation equation and interface condition are

$$\nabla\bullet\boldsymbol{J} = 0, \quad \boldsymbol{N}\bullet[\![\,\boldsymbol{J}\,]\!] = 0 \tag{2.12}$$

and must be imposed in addition to Hamilton's principle for simulating the EMF processes of interest here.

2.2 Material constitutive behavior

To solve the governing Eqs. (2.8), (2.11), and (2.12), the electromagnetic and mechanical material constitutive laws are needed. In addition, since ψ will depend also on internal variables, evolution laws for the internal variables are necessary.

2.2.1 Electromagnetic constitutive response

Recalling that magnetization and polarization are assumed to be negligible, one need specify an electromagnetic constitutive law for $\boldsymbol{J}$ only. The present work assumes an isotropic Ohm's law with constant conductivity σ, given in the reference configuration by:

$$\boldsymbol{J} = \sigma J \boldsymbol{C}^{-1} \bullet \boldsymbol{E}. \tag{2.13}$$

2.2.2 Mechanical constitutive response

An EMF process imposes high strain rates and large strains on the workpiece, thus requiring the use of a viscoplastic constitutive law. The viscoplastic law employed here has been developed independently by the authors (Thomas et al. 2007) for necking experiments in AA6063-T6 tubes—the same aluminum alloy as in the present experiments—and is briefly presented here for the sake of completeness.

In the current configuration, the stress rate is related by elasticity to the elastic part of the strain rate by:

$$\mathring{\boldsymbol{\sigma}}_m = \boldsymbol{\mathcal{L}}^e \overset{\bullet}{\bullet} \boldsymbol{D}^e, \tag{2.14}$$

where $\mathring{\boldsymbol{\sigma}}_m$ denotes the convected rate of the mechanical Cauchy stress $\boldsymbol{\sigma}_m$ (to be subsequently specified), $\mathcal{L}^e$ are the solid's elastic moduli and $\boldsymbol{D}^e$ are the elastic components of the strain-rate tensor. The frame-invariant stress rate $\mathring{\boldsymbol{\sigma}}_m$ is given in terms of the stress rate $\dot{\boldsymbol{\sigma}}_m$ by:

$$\mathring{\boldsymbol{\sigma}}_m = \dot{\boldsymbol{\sigma}}_m + \boldsymbol{L}^T \bullet \boldsymbol{\sigma}_m + \boldsymbol{\sigma}_m \bullet \boldsymbol{L}, \tag{2.15}$$

where $\boldsymbol{L}$ is the solid's velocity gradient. Note that the choice of the convected rate of stress is one of the many possible choices of frame–invariant stress rates.

The strain rate may be additively decomposed into elastic $\boldsymbol{D}^e$ and plastic $\boldsymbol{D}^p$ parts, as follows:

$$\boldsymbol{D} = \boldsymbol{D}^e + \boldsymbol{D}^p. \tag{2.16}$$

The plastic part of the strain rate for a viscoplastic solid which is described in terms of only one internal variable ϵ^p—the accumulated plastic strain—is:

$$\boldsymbol{D}^p = \dot{\epsilon}^p \frac{\partial \sigma_e}{\partial \boldsymbol{\sigma}_m}. \tag{2.17}$$

The internal variable ϵ^p determines the size of the material's current yield surface, which is characterized by the equivalent mechanical stress σ_e, and the relation between ϵ^p and the solid's quasi-static uniaxial response $\sigma_m = g\left(\epsilon^p\right)$ is:

$$\dot{\epsilon}^p = \dot{\epsilon}_0^p \left[\left(\frac{\sigma_e(\boldsymbol{\sigma}_m)}{g\left(\epsilon^p\right)} \right)^{1/m} - 1 \right], \tag{2.18}$$

where the exponent m is the solid's rate-sensitivity exponent and $\dot{\epsilon}_0^p$ is a material constant. Expressions that are based on experiments will be given subsequently for $\sigma_e\left(\boldsymbol{\sigma}_m\right)$ and $g\left(\epsilon^p\right)$.

Attention is now turned to the required kinematical relations. The strain rate $\boldsymbol{D}$ and velocity gradient $\boldsymbol{L}$ are given in terms of the deformation gradient and its rate by:

$$\boldsymbol{D} = \frac{1}{2}\left(\boldsymbol{L} + \boldsymbol{L}^T\right), \quad \boldsymbol{L} = \dot{\boldsymbol{F}} \bullet \boldsymbol{F}^{-1} \tag{2.19}$$

The experimentally motivated (see Yadav et al. 2001) rate-independent uniaxial response of the constitutive law is given by:

$$g\left(\epsilon^p\right) = \sigma_y \left[1 + \frac{\epsilon^p}{\epsilon_y} \right]^n \tag{2.20}$$

where σ_y is the yield stress, $\epsilon_y = \sigma_y / E$ is the yield strain, and n is the hardening exponent.

The mechanical constitutive equations are completed with the yield surface description. The familiar von Mises (isotropic, quadratic) yield surface is employed, which is appropriate for isotropic materials that do not exhibit the Bauschinger effect, and is described in terms of the principal mechanical stresses σ_i by:

$$\sigma_e = \left[\left(|\sigma_1 - \sigma_2|^2 + |\sigma_2 - \sigma_3|^2 + |\sigma_3 - \sigma_1|^2 \right) / 2 \right]^{1/2}. \tag{2.21}$$

Finally, the mechanical Cauchy stress $\boldsymbol{\sigma}_m$ is related to the mechanical portion of the first Piola-Kirchhoff stress $\boldsymbol{\Pi}_m$, defined in (2.10), through:

$$J \boldsymbol{F}^{-1} \bullet \boldsymbol{\sigma}_m = \boldsymbol{\Pi}_m \equiv \rho_0 \left(\frac{\partial \psi}{\partial \boldsymbol{F}} \right)^T, \tag{2.22}$$

which is the standard continuum mechanics relation connecting first Piola–Kirchhoff and Cauchy stress measures.

2.3 Axisymmetric processes

Implementing the aforementioned general theoretical formulation for axisymmetric problems significantly simplifies the formulation (given subsequently in cylindrical coordinates) by reducing the independent variables on the (R, Z) space to three (A_Θ, u_R, u_Z), as discussed in the first subsection (for details on the transformation between current and reference configuration

axisymmetry see Thomas and Triantafyllidis 2009).[4] Special care must be taken with the axisymmetric formulation in the forming coil under a given current, and this is the subject of the second subsection.

2.3.1 Axisymmetric formulation

The forming process of interest is assumed rotationally symmetric (about the Z-axis), implying that no field depends on the Θ coordinate. The corresponding symmetry group is C_∞, i.e. when the solution is invariant to coordinate transformations corresponding to rigid body rotations around the Z-axis. From the assumed symmetry it is expected that there is no hoop displacement ($u_\Theta = 0$), the only nonzero component of the current density and electric field is the hoop component, and the magnetic field thus also has no hoop component ($B_\Theta = 0$). Consequently, for the workpiece and the surrounding free space:

$$\boldsymbol{u} = u_R \boldsymbol{i}_R + u_Z \boldsymbol{i}_Z, \quad \boldsymbol{A} = A_\Theta \boldsymbol{i}_\Theta, \quad \Phi = 0, \\ \boldsymbol{J} = J_\Theta \boldsymbol{i}_\Theta. \tag{2.23}$$

With this formulation in place, it is straightforward to show that the Coulomb gauge condition and charge conservation, plus the corresponding associated interface conditions in the reference configuration, are identically satisfied:

$$\begin{aligned} &\nabla \bullet \boldsymbol{A} = 0, \quad \boldsymbol{N} \bullet [\![\boldsymbol{A}]\!] = 0, \\ &\nabla \bullet \boldsymbol{J} = 0, \quad \boldsymbol{N} \bullet [\![\boldsymbol{J}]\!] = 0. \end{aligned} \tag{2.24}$$

Note that whereas Eqs. $(2.24)_3$ and $(2.24)_4$ must hold in 3-D processes as well, Eqs. $(2.24)_1$ and $(2.24)_2$ are here a result of axisymmetry.

Axisymmetric processes may include applied mechanical body forces $\boldsymbol{f}$ and surface tractions $\boldsymbol{T}$, but neither is needed in the subsequent free electromagnetic tube expansion simulations. The applied mechanical body force $\boldsymbol{f}$ may be ignored since gravity is weak compared to the electromagnetic forces, and there is no applied mechanical surface traction $\boldsymbol{T}$ since the free expansion process involves no contact. Thus, here and subsequently $\boldsymbol{f}$ and $\boldsymbol{T}$ are set to zero.

2.3.2 Forming coil

Though the forming process of interest is assumed to be geometrically axisymmetric, the forming coil in reality must be a continuous spiral. In order to model such a coil in the axisymmetric framework, the formulation must be modified to include the driving electric field. The approach here is similar to that in Stiemer et al. (2006). Each coil turn is approximated as a stationary torus, disconnected geometrically from the other turns. It is required that the electric current density remain axisymmetric, which implies in each coil turn:

$$\boldsymbol{J} = J_\Theta(R, Z)\boldsymbol{i}_\Theta. \tag{2.25}$$

Using Eqs. (2.4), (2.13) and recalling that the coil does not deform (reference and current configuration are the same), one has:

$$J_R = 0 \Rightarrow \frac{\partial \Phi}{\partial R} = A_R = 0, \\ J_Z = 0 \Rightarrow \frac{\partial \Phi}{\partial Z} = A_Z = 0. \tag{2.26}$$

Thus Φ is not a function of R or Z and from Eq. (2.25) J_Θ is not a function of Θ. In view of the potential definitions (2.4) and (2.26), Ohm's law (2.13) takes the form:

$$J_\Theta = -\sigma \left(\frac{1}{R} \frac{\partial \Phi}{\partial \Theta} + \dot{A}_\Theta \right), \tag{2.27}$$

and one deduces in view of Eq. (2.26) that $\partial\Phi/\partial\Theta$ should be a constant. Consequently, ΔU_k, the change in the electric potential over coil turn k is related to Φ by:

$$\frac{\partial \Phi}{\partial \Theta} = \frac{\Delta U_k}{2\pi} \Rightarrow \nabla \Phi = \left(\frac{\Delta U_k}{2\pi R} \right) \boldsymbol{i}_\Theta. \tag{2.28}$$

With this formulation, the electric potential drop in turn k, ΔU_k, can be expressed in terms of the coil current $I(t)$ and the magnetic vector potential A_Θ as follows: Recall from Ohm's law, Eq. (2.13), that since the coil does not deform $\boldsymbol{J} = \boldsymbol{j} = \sigma \boldsymbol{e} = \sigma \boldsymbol{E}$. Integrating over the cross section in the R-Z plane of a coil turn gives the total current in the coil, $I(t)$. Assuming the coil has a rectangular cross section in the R-Z plane aligned with the R-Z axes:

$$\begin{aligned} I(t) &= \int_{S_k} \boldsymbol{J} \bullet \boldsymbol{n}_k \, \mathrm{d}S \\ &= -\sigma \int_{S_k} (\nabla \Phi + \dot{\boldsymbol{A}}) \bullet \boldsymbol{i}_\Theta \, \mathrm{d}S \\ &= -\sigma \int_{S_k} \left(\dot{A}_\Theta + \frac{\Delta U_k}{2\pi R} \right) \mathrm{d}S \\ &= -\sigma \int_{S_k} \dot{A}_\Theta \, \mathrm{d}S - \frac{\sigma h_k}{2\pi} \ln\left(\frac{b_k}{a_k} \right) \Delta U_k, \end{aligned} \tag{2.29}$$

[4] Here and subsequently R, Θ, Z are reference configuration cylindrical coordinates with respective cylindrical unit vectors $\boldsymbol{i}_R, \boldsymbol{i}_\Theta, \boldsymbol{i}_Z$.

where S_k is the surface of the coil's cross section in the R-Z plane, $\boldsymbol{n}_k = \boldsymbol{i}_\Theta$ is the normal to the cross-section, h_k is the height of the cross section, b_k is the outside radius of the cross section and a_k is the inside radius of the cross section. This equation may be solved for ΔU_k in terms of $I(t)$ and $\dot{A}_\Theta$, and using in addition Eqs. (2.4), (2.13) and (2.28) the hoop component electric current density at an arbitrary point (R, Z) in coil turn k is given by:

$$J_\Theta(R, Z) = \frac{\sigma}{h_k R}\left(\ln\left(\frac{b_k}{a_k}\right)\right)^{-1}\left(\frac{I(t)}{\sigma} + \int_{S_k} \dot{A}_\Theta \, \mathrm{d}S\right) - \sigma \dot{A}_\Theta. \tag{2.30}$$

This expression for the electric current density in the coil, along with the variational formulation of Eq. (2.2), yields a boundary value problem dependent only on A_Θ, u_R and u_Z.

3 Numerical implementation

The numerical implementation of the general theory is based on a variational integration method applied to the variational principle introduced in Sect. 2. According to this method, space and time interpolation schemes are concurrently applied to the Lagrangian, followed by the variational principle applied on the discrete nodal variables for each time step. A survey of the extensive literature on this topic may be found in the introductory discussion of Marsden and West (2001). The numerical techniques detailed subsequently are implemented using the finite element program FEAP (2005).

In the axisymmetric problem discussed here, the independent variables, functions of R and Z, are: nonzero magnetic vector potential component A_Θ and nonzero displacement components u_R and u_Z. All the independent variables are continuous functions of the space variables, as discussed in Sect. 2.3. Therefore, employing nodal finite elements for the spatial discretization, one has:

$$\begin{aligned} \boldsymbol{A}_e(R, Z; t) &\approx \boldsymbol{M}(R, Z) \bullet \boldsymbol{q}_e(t), \\ \boldsymbol{u}_e(R, Z; t) &\approx \boldsymbol{N}(R, Z) \bullet \boldsymbol{p}_e(t), \end{aligned} \tag{3.1}$$

where $\boldsymbol{A}_e$ is the vector potential $\boldsymbol{A}$ inside an element, $\boldsymbol{M}$ is the spatial interpolation matrix of element basis functions for $\boldsymbol{A}_e$, $\boldsymbol{q}_e$ are the nodal degrees of freedom for $\boldsymbol{A}_e$, $\boldsymbol{u}_e$ is the displacement $\boldsymbol{u}$ inside an element, $\boldsymbol{N}$ is the spatial interpolation matrix of element basis functions for $\boldsymbol{u}_e$ and $\boldsymbol{p}_e$ are the nodal degrees of freedom for $\boldsymbol{u}_e$. Four node bilinear quadrilateral elements are used to discretize $\boldsymbol{A}$ and $\boldsymbol{u}$, with the same mesh being employed for each variable. These linear elements are appropriate since the Lagrangian, Eq. (2.1), involves only up to first derivatives of continuous functions $\boldsymbol{A}$ and $\boldsymbol{u}$.

Using the backward Euler approximation for time discretization, one obtains:

$$\begin{aligned} \dot{\boldsymbol{A}}_e(R, Z; t^i) &\approx \boldsymbol{M}(R, Z) \bullet \dot{\boldsymbol{q}}_e(t^i), \\ \dot{\boldsymbol{q}}_e(t^i) &\approx \frac{\boldsymbol{q}_e^i - \boldsymbol{q}_e^{i-1}}{\Delta t}, \\ \dot{\boldsymbol{u}}_e(R, Z; t^i) &\approx \boldsymbol{N}(R, Z) \bullet \dot{\boldsymbol{p}}_e(t^i), \\ \dot{\boldsymbol{p}}_e(t^i) &\approx \frac{\boldsymbol{p}_e^i - \boldsymbol{p}_e^{i-1}}{\Delta t}, \end{aligned} \tag{3.2}$$

where $\boldsymbol{q}_e^i$ and $\boldsymbol{p}_e^i$ are the degrees of freedom in an element at time t^i and where the time step $\Delta t \equiv t^i - t^{i-1}$.

With the above space and time discretization and using linear interpolation rule for the time integration of $\mathscr{F}$, its corresponding discrete counterpart $\mathscr{F}^d$ is found to be:

$$\begin{aligned} \mathscr{F} &\equiv \int_{t^0}^{t^M} \mathscr{L}(\boldsymbol{A}, \boldsymbol{u}, \dot{\boldsymbol{u}}) \, \mathrm{d}t \\ &\approx \Delta t \sum_{i=1}^{M} \mathscr{L}_i^d(\boldsymbol{q}^i, \boldsymbol{p}^{i-1}, \boldsymbol{p}^i) \equiv \mathscr{F}^d, \end{aligned} \tag{3.3}$$

where the Lagrangian is given in Eq. (2.1) and its discrete approximation at time t^i, $\mathscr{L}_i^d(\boldsymbol{q}^i, \boldsymbol{p}^{i-1}, \boldsymbol{p}^i)$, follows from applying the discretization Eqs. (3.1) and (3.2) and using a 2×2 Gauss numerical quadrature for spatial integration. Also, $\boldsymbol{q}^i$ and $\boldsymbol{p}^i$ are the nodal degrees of freedom at time t^i throughout the space domain. Upon application to $\mathscr{F}^d$ of Hamilton's variational principle with respect to these degrees of freedom, the discretized governing equations are:

$$\mathscr{F}^d_{,\boldsymbol{q}^i}\left[\delta \boldsymbol{q}^i\right] = 0, \quad \mathscr{F}^d_{,\boldsymbol{p}^i}\left[\delta \boldsymbol{p}^i\right] = 0. \tag{3.4}$$

These equations provide the time stepping routine to solve for the degrees of freedom at each time step, i.e. given $[\boldsymbol{q}^{i-1}, \boldsymbol{q}^i, \boldsymbol{p}^{i-1}, \boldsymbol{p}^i]$ one calculates $[\boldsymbol{q}^{i+1}, \boldsymbol{p}^{i+1}]$. The time stepping routine for $\boldsymbol{q}$ is a result of applying Eqs. (2.4), (2.13), and $(3.2)_2$ after variational integration, recalling also that $\boldsymbol{J}$ is a driving force in the variational principle and must be related to the independent

fields through a constitutive relation. The choice of spatial and time interpolations in Eqs. (3.1) and (3.2) and the space and time integration algorithms used for (3.3), respectively, result in implicit time integration for $\boldsymbol{q}$ and explicit time integration for $\boldsymbol{p}$. At each time step the finite element problem is:

$$\begin{aligned} &\boldsymbol{R} \bullet \boldsymbol{p}^{i+1} = \boldsymbol{f}_p(\boldsymbol{q}^i, \boldsymbol{p}^{i-1}, \boldsymbol{p}^i) \Rightarrow \boldsymbol{p}^{i+1} = \boldsymbol{R}^{-1} \bullet \boldsymbol{f}_p, \\ &\boldsymbol{K}(\boldsymbol{p}^{i+1}) \bullet \boldsymbol{q}^{i+1} = \boldsymbol{f}_q(\boldsymbol{q}^i, \boldsymbol{p}^{i+1}; t^{i+1}), \end{aligned} \tag{3.5}$$

where $\boldsymbol{R}$ is the constant mass matrix associated with the mechanical degrees of freedom, $\boldsymbol{f}_p$ is the force vector associated with the mechanical degrees of freedom, $\boldsymbol{K}$ is the tangent matrix associated with the electromagnetic degrees of freedom and $\boldsymbol{f}_q$ is the force vector associated with the electromagnetic degrees of freedom. One may calculate nodal displacements $\boldsymbol{p}^{i+1}$ from Eq. $(3.5)_1$ where the mass matrix $\boldsymbol{R}$ is constant. Then the nodal vector potential $\boldsymbol{q}^{i+1}$ is given in terms of $\boldsymbol{q}^i$ and $\boldsymbol{p}^{i+1}$ by Eq. $(3.5)_2$ where the tangent matrix $\boldsymbol{K}(\boldsymbol{p}^{i+1})$ depends on the current geometry. Note that the resulting scheme is an efficient staggered solution algorithm with two uncoupled solution steps, neither of which requires an iterative solution technique.

In addition to solving for the nodal variables $\boldsymbol{p}^i$ and $\boldsymbol{q}^i$, the evolution law for the internal variable ϵ^p must be integrated. The evolution equations are local and depend only on the history at each integration point. Moreover, by the construction of internal variables the free energy depends only on the internal variable itself rather than its rate, i.e. in the present model we have $\psi(\boldsymbol{u}, \epsilon^p)$. Therefore at each time step the evolution law can be integrated separately from the governing equations of the boundary value problem. To do so, a fourth order Runge-Kutta scheme is employed within each time interval to find ϵ^p, as in Thomas and Triantafyllidis (2007).

To complete the implementation the initial and boundary conditions are needed. The initial conditions are given by:

$$\boldsymbol{A} = \boldsymbol{0}, \quad \boldsymbol{u} = \boldsymbol{0}, \quad \dot{\boldsymbol{u}} = \boldsymbol{0} \quad \text{at} \quad t = 0. \tag{3.6}$$

Note that the problem is driven by the time dependent input electric current $I(t)$, as discussed in Sect. 2.3.2.

The problem also requires application of the essential boundary conditions. In addition to axisymmetry, the processes modeled subsequently will all have mirror symmetry about $Z = 0$. This implies the essential boundary conditions for $\boldsymbol{A}$ are:

$$\begin{aligned} &A_\Theta = 0 \quad \text{at} \quad R = 0, \\ &A_\Theta \to 0 \quad \text{as} \quad R^2 + Z^2 \to \infty, \end{aligned} \tag{3.7}$$

since rotational symmetry implies that $A_\Theta = 0$ on the axis $R = 0$ and the electromagnetic fields decay to zero at infinity. For simplicity, the latter boundary condition is implemented by taking a large area of meshed air and applying $A_\Theta = 0$ at the edges. In the following calculations it has been confirmed that the size of the air mesh is large enough as to accurately model the infinity boundary condition. For $\boldsymbol{u}$, we need to impose only the boundary conditions:

$$\begin{aligned} &u_R = 0 \quad \text{at} \quad R = 0, \\ &u_Z = 0 \quad \text{at} \quad Z = 0, \end{aligned} \tag{3.8}$$

which are dictated by rotational symmetry about $R = 0$ and mirror symmetry about $Z = 0$ respectively.

Note that outside the workpiece the displacements are not uniquely determined by the variational procedure. The coil is stationary, and in the surrounding air the equation of motion is satisfied identically, as expected. However, it is necessary to assume a kinematically admissible displacement field in the air in order to ensure the mapping between reference and current configurations remains invertible, i.e. a nonsingular $\boldsymbol{K}(\boldsymbol{p}^{i+1})$ in Eq. (3.5). Moreover, this distribution affects the numerical solution and if not carefully chosen can cause the simulation to give poor results. In the present work, a simple linear distribution of displacements in the air is implemented that adjusts with the displacements in the workpiece as necessary (see Sect. 5).

Finally, it is also important to note the influence of the forming coil on the numerical algorithm. Equation (2.30) implies that each degree of freedom $\boldsymbol{q}_e$ in a coil turn cross section is directly coupled to its counterparts on the same coil cross section. This introduces non-local relations into the finite element method and the resulting tangent matrix $\boldsymbol{K}$ in Eq. (3.5) is asymmetric.

4 Experimental procedure

A schematic of the instrumented electromagnetic tube expansion experiments is shown in Fig. 1. The power

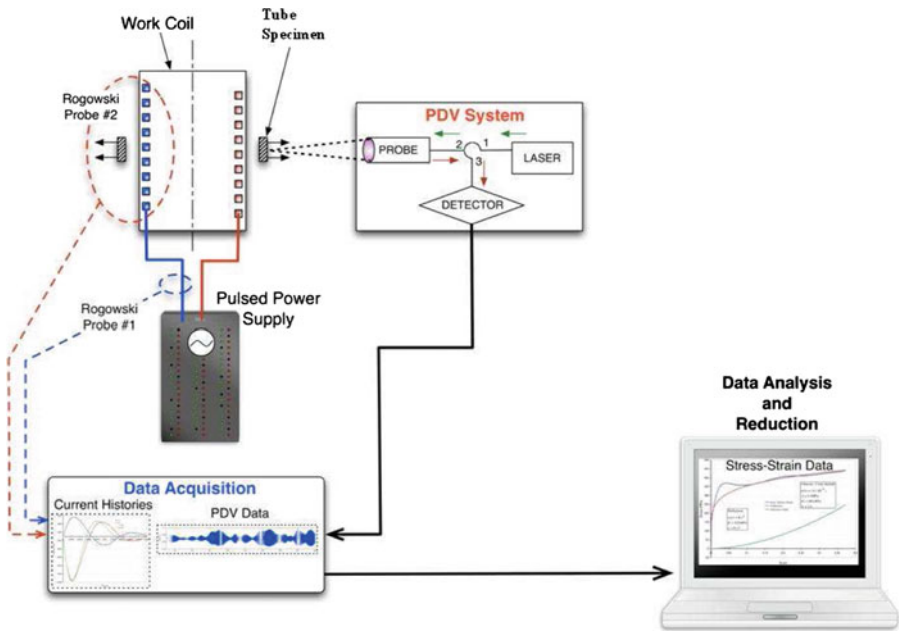

Fig. 1 Schematic of the experimental set-up for the electromagnetically induced free expansion of AA6063-T6 aluminum alloy tubes with instrumentation for measurement of electric currents and rate of expansion (Johnson et al. 2009)

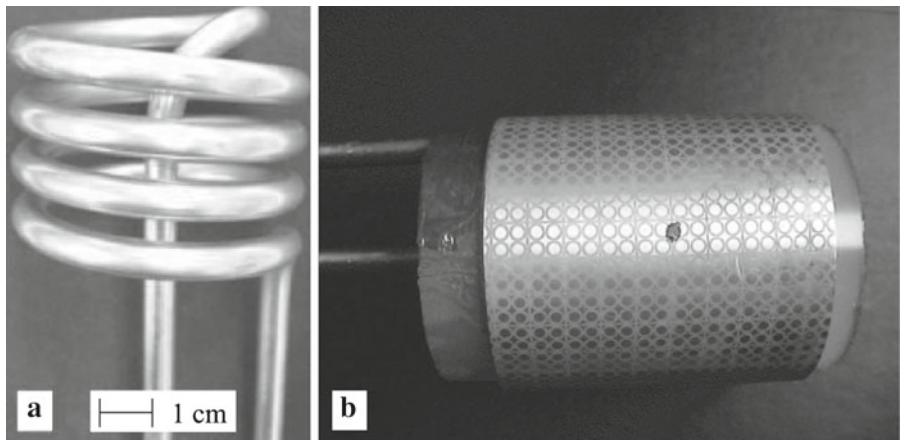

Fig. 2 **a** The bare 4-turn coil. **b** Sample-actuator configuration. An aluminum tube sample is shown fitted around the urethane-coated 4-turn coil

supply is a Magneform capacitor bank with a nominal maximum capacity of 16 kJ at its nominal charging voltage of 8.66 kV. This unit has a total capacitance of 426 μF, has an internal inductance of about 100 nH and is switched by 8 ignitron switches that are located on each of the bank's eight capacitors. In principle the banks total capacitance can be decreased by removing capacitors from the circuit, but in this study all eight capacitors were engaged in the circuit for each experiment. As shown in Fig. 1, Rogowski probe #1 measures the primary (i.e. forming circuit) current. The secondary (i.e. workpiece) current is measured indirectly using Rogowski probe #2, which measures the sum of the secondary current and the total primary current in all the coil turns. Figure 2a shows a four turn brass work coil fabricated by commercial spring winding from 6.43 mm diameter ASTM B16 brass wire. The coil has a diameter of 54 mm and a pitch of 10.5 mm. The wire is covered with heat-shrink wrap tubing to provide insulation and then potted in urethane.

Figure 2b shows the actual experimental configuration of an AA6063-T6 tube sample fitted over the epoxy-coated coil. (The tubes were electrolytically etched with a pattern of 2.5 mm circles in order to measure strains in the expanded tubes if desired.) The tube samples had an inner diameter of 57 mm, a thickness of

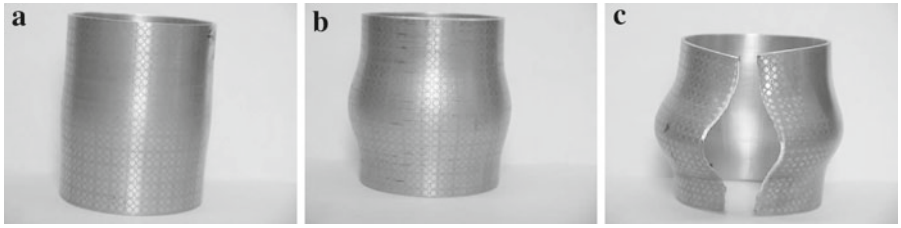

Fig. 3 Final configuration of the tubes expanded at **a** 4.8 kJ **b** 6.4 kJ **c** 7.2 kJ using the experimental EMF set-up with a 4-turn coil

1.49 mm and a height of 72.9 mm, making them much taller than the coil. The tubes were expanded at 4.8, 6.4, 7.2 and 9.6 kJ energy levels to find the threshold energy for necking. The expanded tubes of the first three energies are shown in Fig. 3a,b and c respectively. At 9.6 kJ catastrophic failure occurred and the tube broke into multiple pieces. Upon finding that 6.4 kJ is the threshold energy level the experiment was repeated thrice at that level with full instrumentation.

The rates of expansion of diametrically opposite points on the tube mid-section (e.g. see the marked point in Fig. 3b) were measured using Photon Doppler Velocimetry, the basic principle for which is shown in Fig. 4. This technique has been developed by Strand et al. (2005) and is based on the interference of original and Doppler shifted laser reflected from a moving object. The system mainly consists of a 1 watt 1,550 nm erbium fiber laser, probe (typically a focuser), high speed-high frequency oscilloscope and optical detector. When the shifted and unshifted lasers interfere in the detector they produce beats whose frequency is directly proportional to the speed at which the target (in this case, the tube) is moving. The time gap between each crest of the beat signal is the time taken for the target to move half the wavelength of the laser signal, which is 1,550 nm. A simple fast-Fourier transform technique is used to convert the beat intensity signal into velocity versus time data. This data is then integrated to find the radial displacement at the particular point on the tube.

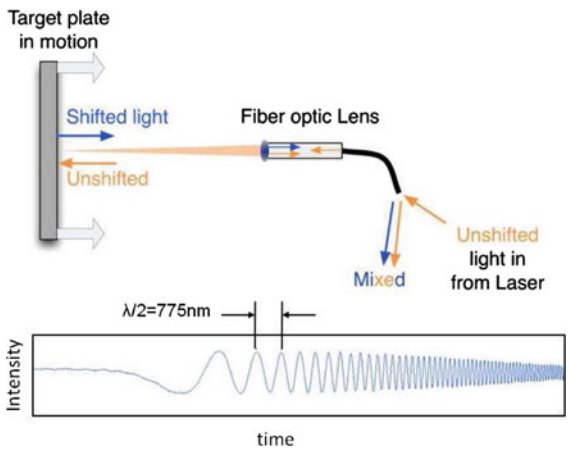

Fig. 4 Illustration of the basic principle of the Photon Doppler Velocimeter and an example experimental trace. Shifted light reflected off the moving target interferes with unshifted light reflected off the lens to produce beats in the mixed signal, as shown in the experimental data at the bottom

5 Results and discussion

We now turn to comparison of simulation and experiment. The ensuing simulations of electromagnetically driven, freely expanding tubes use the geometries, material properties and input electric currents of the experiments discussed in the previous section. The experimentally measured tube electric current and tube mid-section displacement are compared with the simulation results.

The experimental set-up geometry used for the calculations is shown schematically in Fig. 5a, where the coil is idealized as axisymmetric rings. Figure 5b shows the simulation domain (top right quarter of the plane $\Theta = 0$) with the relevant dimensions. The mid-points of the coil turns and tube section are denoted with solid dots, and the mid-line of the tube section is denoted with a dashed line. The relevant dimensions are: radius of the coil sections mid-points, R_c; radius of tube section mid-line, R_t; distance between two adjacent coil turns, P_c; one half height of the tube, Z_t; coil turn cross section thickness, T_c; and tube cross section thickness, T_t. Note that the coil dimensions from Sect. 2.3.2 are thus $h_k = T_c, a_k = R_c - T_c/2$, and $b_k = R_c + T_c/2$.

This section starts with a presentation of the meshing and time steps, followed by the choice of constitutive properties and proceeds with the comparison of experimental and simulation results.

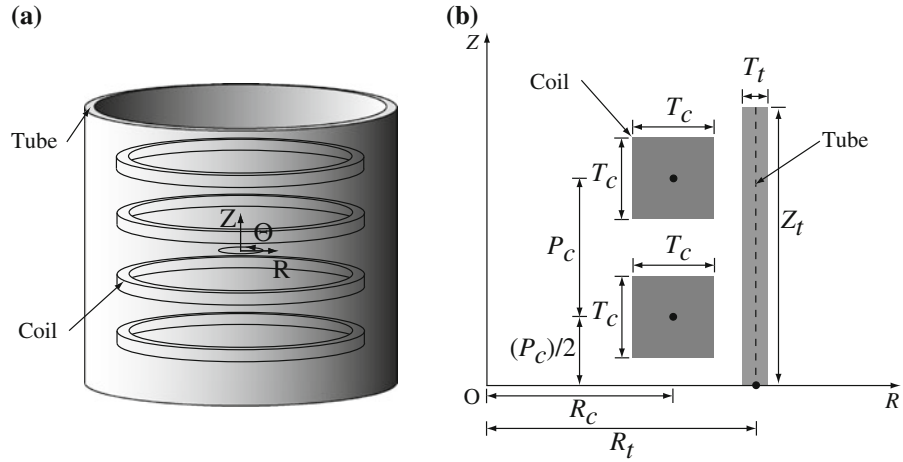

Fig. 5 **a** Idealized tube expansion set-up. **b** Simulation domain and dimensions

5.1 Meshing and time step selection

The reference configuration finite element mesh is for simplicity a distorted Cartesian grid. Figure 6 shows a typical finite element mesh of an EMF tube expansion problem (a shorter tube is meshed in this figure for illustration convenience, since the tubes used in the experiments are much taller than the coil). The tube and coil are depicted in dark grey, and the air is depicted in white and light grey. We use four elements in each square coil turn and 460 elements in the tube. The result is 5915 nodes in the simulation domain.

There are two regions of air mesh: one that moves during the process with assigned displacements (necessary near the tube, as noted in Sect. 3) and one fixed. The air region in light grey in Fig. 6 has displacements that vary linearly from those on the tube surface to zero on the boundary of the region. This region covers, in the R direction, from the outside radius of the coil ($R = R_c + T_c/2$) to a distance ΔR^d_{mesh} beyond the outside of the tube and, in the Z direction, from $Z = 0$ to a distance ΔZ^d_{mesh} beyond the top of the tube. The remaining air in the simulation domain (in white in Fig. 6) is fixed, and the simulation domain extends beyond the region with non-zero air displacements distances of ΔR_{mesh} and ΔZ_{mesh} in the R and Z directions, respectively. These dimensions, which are labeled in Fig. 6, are chosen relative to the inner radius of the tube, $R^{\text{in}}_t = R_t - T_t/2$. Based on convergence studies, all the subsequent simulations use $\Delta R^d_{\text{mesh}} = \Delta Z^d_{\text{mesh}} = R^{\text{in}}_t$ and $\Delta R_{\text{mesh}} = \Delta Z_{\text{mesh}} = 10R^{\text{in}}_t$. Finer meshes were also used for convergence studies and showed negligible change in the results, thus justifying the use of the above described mesh for the simulations reported here.

The time step Δt is chosen for stability and accuracy, which are affected by the elastic wave speed (and thus the size of the elements in the tube) and characteristic time of the electric current pulse. The need to resolve elastic waves is the limiting factor, though the characteristic time of the electric current pulse controls the macroscopic deformation. From convergence studies it was found that decreasing the time step below the value we ended up using, i.e. $\Delta t = 5 \times 10^{-9}$ s, showed negligible change in the solution.

5.2 Selection of material constants

In the interest of simplicity temperature effects are ignored. The adopted electromagnetic and mechanical material response parameters are discussed below.

5.2.1 Electromagnetic constitutive parameters

Ohm's law is required to relate electric current density with electric field, and its constant conductivity version is given in Eq. (2.13). The resistivity (resistivity $r = 1/\sigma$) of aluminum, r_{Al} (the experimental tubes were made of AA6063-T6 aluminum alloy), and brass, r_{Br} (the actuator was made of ASTM B16 brass), have been obtained from standard tables. The values of the electromagnetic constitutive parameters (which in addition to the resistivities include the permeability of vacuum μ_0) are given in Table 1.

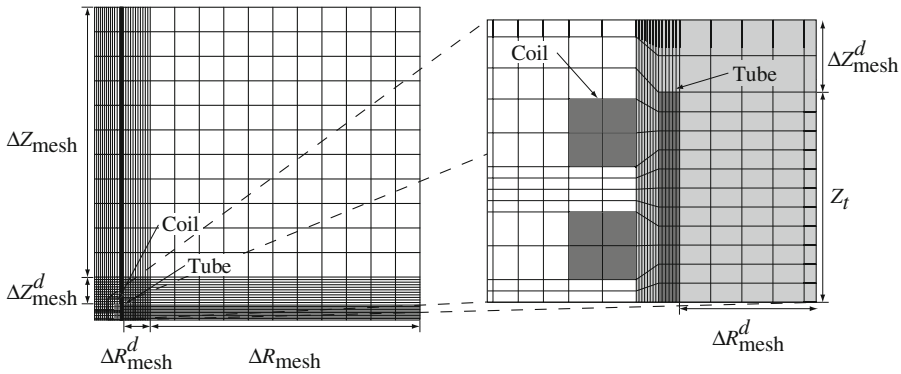

Fig. 6 Sample finite element mesh for axisymmetric tube expansion with a near–coil domain magnification

Table 1 Electromagnetic constitutive parameter values used in simulations

$\mu_0 = 1.26 \times 10^{-6}$ N/A^2	$r_{Al} = 2.65 \times 10^{-8} \Omega$m	$r_{Br} = 6.6 \times 10^{-8} \Omega$m

Table 2 Mechanical constitutive parameter values used in simulations

$E = 69 \times 10^9$ Pa	$\sigma_y = 190 \times 10^6$ Pa	$\epsilon_y = \sigma_y / E$	$n = 0.0769$
$m = 0.0870$	$\dot{\epsilon}^p_0 = 1,000\,\text{s}^{-1}$	$\nu = 0.3$	$\rho_0 = 2,700\,\text{kg/m}^3$

5.2.2 Mechanical constitutive parameters

The mechanical constitutive law employed for the tubes is the viscoplastic model presented in Sect. 2. The power law of Eq. (2.20) was fit by Thomas et al. (2007) for the tube alloy AA6063-T6. The resulting Young's modulus E, yield stress σ_y, yield strain ϵ_y and hardening exponent n are given in Table 2. The rate parameters strain rate sensitivity exponent m and material parameter $\dot{\epsilon}^p_0$ also used in Thomas et al. (2007); Thomas and Triantafyllidis (2007) are based on experiments by Yadav et al. (1995, 2001) on the closely related alloy AA6061-T6. Poisson's ratio ν and the reference configuration mass density ρ_0 also shown in Table 2 are obtained from standard tables on Aluminum, since they are not alloy sensitive.

With the constitutive laws in place, we now proceed to comparison of electromagnetic tube expansion experiment and simulation.

5.3 Comparison of experiment and simulation

As discussed in Sect. 4, once the capacitor energy was found at which the tubes expanded until just before localization, three tubes were expanded at this energy. Each tube had the movement of two diametrically opposite points on its mid-section, labeled C1 and C2, measured with Photon Doppler Velocimetry. The location of points C1 and C2, relative to the forming coil, stayed fixed. Three quantities were available experimentally: primary (i.e. forming coil) electric current, secondary (i.e. tube) electric current and displacement of points on the tube mid-section (calculated from the measured data). In the following figures, the experimental data for each measured quantity are presented first, followed by a second figure with the average of the same experimentally measured quantity plus the corresponding simulation result.

Table 3 Geometry of tube expansion simulations

$R_c = 0.023785\,\text{m}$	$P_c = 0.0105\,\text{m}$	$T_c = 0.00569844\,\text{m}$
$R_t = 0.029375\,\text{m}$	$Z_t = 0.036467\,\text{m}$	$T_t = 0.0014933\,\text{m}$

The geometry of the tube expansion simulations is given in Table 3. Each coil turn has a square cross section with the same area as the circular cross sections of the coils in the experiments (square cross sections simplify meshing of the coil).

The experimentally measured primary electric currents are shown in Fig. 7. Note that here and subsequently we have ignored a portion of one of the experimental primary current curves prior to the first peak due to large spurious oscillations that appeared in the data, an undesirable intermittent artifact of the experimental

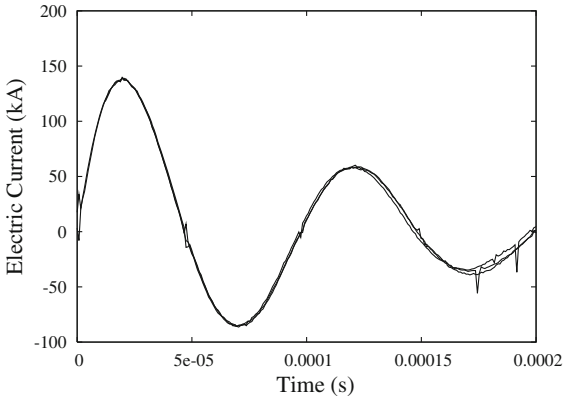

Fig. 7 Experimentally measured primary (i.e. forming coil) electric current for the tube expansion experiments

Table 4 Input electric current parameters

$I_0 = 133 \times 10^3$ A	$t_0 = 24 \times 10^{-6}$ s	$k_1 = 0.4$	$k_2 = 0.64$

measurement apparatus. Since in the experiments the electric current in the forming coil is very close to an exponentially decaying sinusoid, the general form taken in the present work is (a slightly modified version of that in Thomas and Triantafyllidis 2009):

$$I(t) = \begin{cases} \text{For } t < 2t_0: \\ \quad I_0 \sin\left(\dfrac{\pi t}{2t_0}\right) \exp\left(\ln(k_1)\left(\dfrac{t}{2t_0}\right) - \dfrac{\ln(k_1)}{2}\right), \\ \text{For } t > 2t_0: \\ \quad I_0 \sin\left(\dfrac{\pi t}{2t_0}\right) \exp\left(\ln(k_2)\left(\dfrac{t}{2t_0}\right) - \dfrac{\ln(k_2)}{2}\right), \end{cases} \tag{5.1}$$

where $2t_0$ is the characteristic time of the current pulse, I_0 is the characteristic electric current and k is a decay parameter. This general form is found to give a satisfactory fit to the experimentally measured data using the parameters given in Table 4, as shown in Fig. 8.

The secondary current was also measured for each expanded tube, and the experimental data are given in Fig. 9.

Unfortunately, due to an experimental measurement error for one tube, only two induced current curves are available.

A comparison of the calculated simulation secondary current and average experimental secondary current is in Fig. 10.

It is clear that the secondary currents agree quite well, especially considering the geometric idealization adopted for the coil, i.e. an axisymmetric (rings)

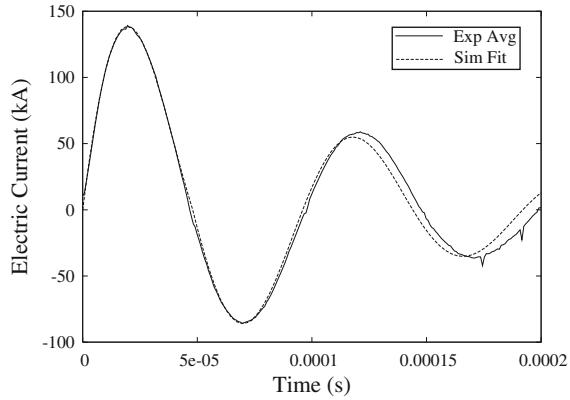

Fig. 8 Comparison of experiment average and analytic fit for primary (i.e. forming circuit) electric current

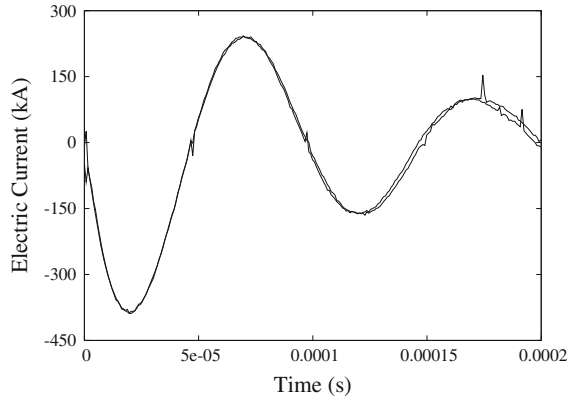

Fig. 9 Experimentally measured secondary (i.e. tube) electric current for the tube expansion experiments

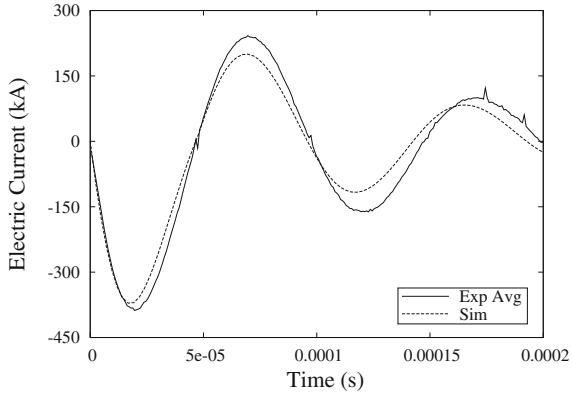

Fig. 10 Comparison of experimental average and simulation for the secondary (i.e. tube) electric current

configuration instead of the actual non-axisymmetric (helical) one.

The displacement versus time obtained from the measured data for each expanded tube is given in

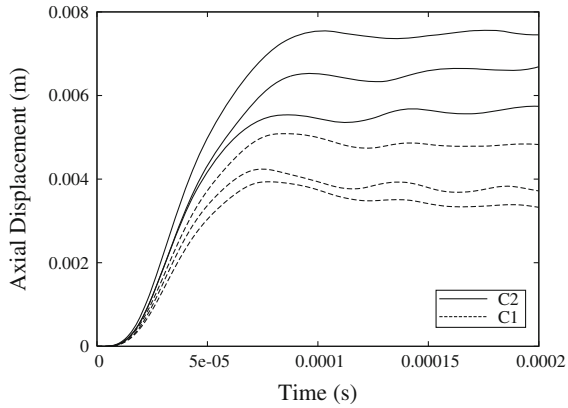

Fig. 11 Tube mid-section displacement calculated from the C1 and C2 probe data of the three tube expansion experiments

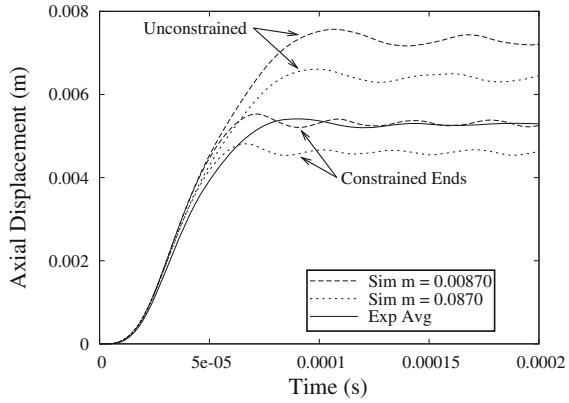

Fig. 12 Comparison of experiment average and simulation mid-section displacement for two values of the strain rate hardening exponent m and two types of tube end constraint

Fig. 11, where there are three curves for each of the measurement points C1 and C2.

Note that the displacements at C2 were consistently higher than at C1, which can be explained by the placement of the measurement points 180° apart on the mid-section of a tube with a non-axisymmetric coil. The significant variation between the different experiments can, in addition to the non-axisymmetry, be attributed to the variation of tube heights (from 72.5 to 73.2 mm) and tube average wall thicknesses (from 1.44 to 1.59 mm). There was also significant variation in each tube's wall thickness (up to 11% of the average). To minimize the influence of the helical coil, we will average the displacements of the two diametrically opposite points for each experiment and subsequently average this result over the three experiments.

A comparison of the average experimental and calculated tube mid-section displacement is in Fig. 12. The curves labeled "$m = 0.0870$" use the value of the strain rate sensitivity exponent m that has been employed for calculations involving the same alloy by Thomas et al. (2007); Thomas and Triantafyllidis (2007). The curves labeled "$m = 0.00870$" use a rate sensitivity exponent one tenth of the previous value and correspond to an essentially quasi-static response (this being the most convenient way to obtain quasi-static response with a viscoplastic model, since further lowering of the rate sensitivity exponent showed no significant change in the results). The maximum experimental tube expansion velocities, around 150 m/s, gave rise to strain rates of about 2,500 s^{-1}. This is in the range at which strain rate sensitivity begins to influence the constitutive response in Aluminum alloys (Vural et al. 2004), so both values of m are of interest for the present investigation.

The set of curves labeled "Unconstrained" in Fig. 12 are the result of free expansion simulations with no constraints on the tube ends. In the experiments there was considerable contact between the tube ends and coil epoxy casing, evidenced by the observation of a tight, almost immovable fit between the coil casing and specimens after deformation. Moreover, the free expansion simulations showed small but significant inward displacement of the tube ends (the outward Lorentz forces are concentrated near the coil and essentially zero at the tube ends). If the simulations had modeled the coil casing (it is electromagnetically transparent) and contact, this motion would have caused tube-casing interaction. To assess the effect of this contact, the "Constrained Ends" curves are included, in which we fully constrain the nodes on the tube inside surface at the top and bottom 5% of the tube's height. This is a simple way to simulate the constrained, high friction end conditions.

The mid-section displacement in the free expansion simulations significantly over predicts the deformation, as seen in Fig. 12, in particular predicting higher expansion velocity, but the results are within the experimental variation. The simulation curves essentially mirror the experimental results but with larger displacements, and the free expansion simulations show oscillations after reaching a maximum displacement, due to elastic vibrations about the final plastically deformed state, that the experiments confirm. The experimental oscillations show similar frequency but lower amplitude; the

reason suspected for this discrepancy is the presence of frictional contact between tube and epoxy casing of the coil.

We expect the presence of tube-coil casing contact and friction to produce tube midline deformation lower than for free expansion. This is seen in Fig. 12 where the "Constrained Ends" computational results agree much more closely with the experimental results. However, the expansion velocity is still overpredicted and the constraints increase the frequency of the elastic vibrations to higher than that experimentally observed. This indicates other aspects of the experiments are still not captured, potentially including the exact behavior of tube-coil casing contact, inefficiencies due to asymmetry relative to perfect axisymmetry and effects of experimental specimen variability. Nevertheless, it is encouraging that the mid-section displacement shows good agreement between simulation and experiment at the initial and final stages of the deformation. It is noteworthy that the agreement between experiment and simulation for the final displacement is considerably better for the almost quasi-static model, thus giving support to the argument of Zhang et al. (2008), Zhang and Ravi-Chandar (2006, 2008) that rate sensitivity is not relevant for the alloys used and at the speeds involved in EMF.

The present experiments should be viewed as a *first attempt* to compare time-dependent electric and mechanical measurements in EMF with calculations based on a unified variational principle. Two main limiting factors of the simulations are axisymmetry (where in fact a helical coil was used) and absence of contact between tube and coil casing (inevitable for tubes considerably taller than coil). We also have not investigated the effect of heat generation here, though previous work on similar forming cases (Thomas et al. 2007) indicates modest temperature changes (less than 100 K) are to be expected, which would not significantly affect the present simulations.

On the other hand there was no adjustable parameter in the simulations; the material properties of the alloy were obtained independently for the same alloy—from a different work—as were all the electrical properties and geometric data. The induced electric currents were predicted very well by the simulations. Moreover, we used averaging of displacements from two diametrically opposed points on the tube's mid-section to mitigate any systematic error of the measurements. The average displacement is over predicted, but the simulation is within experimental variation. Moreover, including the effects of friction increases experiment-simulation agreement, indicating some over prediction is to be expected. The model also predicts the period—but not quite the amplitude—of the ensuing elastic oscillations. The present work gives us confidence in the simulation method proposed and will be employed in simulating further experiments under way in electromagnetically loaded tubes with full-field, time-dependent measurements of surface strains.

6 Conclusion

The present work is motivated by the desire to understand Electromagnetic Forming (EMF) methods, which use electromagnetic (Lorentz) body forces to shape metallic parts and which are finding significant new applications in fracture and fragmentation research as well as in manufacturing processes. Of particular interest here is the simulation of time-dependent deformations and electric currents in electromagnetically loaded solids. In contrast to previous work on modeling similar experiments, the novel feature of this work is the use of a recently developed (Thomas and Triantafyllidis 2009), fully coupled variational formulation which results in an efficient numerical algorithm, based on variational integration. In addition, the present simulation employs a viscoplastic mechanical constitutive response for the workpiece, which has been developed independently for the aluminum alloy used in the present experiments.

A number of free expansion experiments were performed on AA6063-T6 aluminum tubes, during which electric currents and tube mid-plane displacements (obtained by Photon Doppler Velocimetry) were measured as functions of time. The results show a reasonable agreement between simulation and experiment, predicting many experimental features and confirming that the new formulation proposed by Thomas and Triantafyllidis (2009) provides a useful foundation for the study of many interesting problems in the rapidly growing area of coupled electromagnetic-mechanical processes.

Acknowledgments The authors gratefully acknowledge support from the National Science Foundation, grant CMMI 0900 007, and General Motors Research and Development. The authors also acknowledge many helpful discussions with

Professor K. Ravi-Chandar of the Aerospace Engineering and Engineering Mechanics Department at the University of Texas at Austin and Dr. Pierre L'Eplattenier of Livermore Software Technology Corporation.

References

Balanethiram V, Daehn G (1992) Enhanced formability of interstitial free iron at high strain rates. Scripta Metall et Mater 27:1783–1788

Balanethiram V, Daehn G (1994) Hyperplasticity: increased forming limits at high workpiece velocity. Scripta Metall et Mater 31:515–520

El-Azab A, Garnich M, Kapoor A (2003) Modeling of the electromagnetic forming of sheet metals: state-of-the-art and future needs. J Mater Process Technol 142:744–754

FEAP (2005) Finite Element Analysis Program. University of California at Berkeley (Civil and Environmental Engineering). Available at http://www.ce.berkeley.edu/~rlt/feap/

Fenton GK, Daehn GS (1998) Modeling of electromagnetically formed sheet metal. J Mater Process Technol 75:6–16

Hu XY, Daehn GS (1996) Effect of velocity on flow localization in tension. Acta Mater 44(3):1021–1033

Imbert JM, Winkler SL, Worswick MJ, Oliveira DA, Golovashchenko SF (2005) The effect of tool-sheet interaction on damage evolution in electromagnetic forming of aluminum alloy sheet. J Eng Mater Technol Trans ASME 127:145–153

Imbert J, Worswick M, Winkler S, Golovashchenko S, Dmitriev V (2005a) Analysis of the increased formability of aluminum alloy sheet formed using electromagnetic forming. In: Sheet/Hydro/Gas Forming Technology and Modeling 2005. SAE International

Johnson JR, Taber G, Vivek A, Zhang Y, Golowin S, Banik K, Fenton GK, Daehn GS (2009) Coupling experiment and simulation in electromagnetic forming using photon doppler velocimetry. Steel Res Int 80:359–365

Kamal M, Daehn GS (2007) A uniform pressure electromagnetic actuator for forming flat sheets. J Manuf Sci Eng 129:369–379

Karch C, Roll K (2005) Transient simulation of electromagnetic forming of aluminum tubes. Adv Mater Res 6–8: 639–648

Kleiner M, Brosius A, Blum H, Suttmeier F, Stiemer M, Svendsen B, Unger J, Reese S (2004) Benchmark simulation for coupled electromagnetic-mechanical metal forming processes. Ann Ger Soc Prod Technol XI/1:85–90

Kovetz A (2000) Electromagnetic theory. Oxford University Press, Oxford

Lax M, Nelson D (1976) Maxwell equations in material form. Phys Rev B 13(4):1777–1784

L'Eplattenier P, Cook G, Ashcraft C, Burger M, Shapiro A, Daehn G, Seth M (2006) Introduction of an electromagnetism module in LS-DYNA for coupled mechanical-thermal-electromagnetic simulations. In: Proceedings from 9th international LS-DYNA users conference. Livermore Software Technology Corp. Dearborn, MI

Marsden JE, West M (2001) Discrete mechanics and variational integrators. Acta Numer 10:357–514

Maugin GA (1988) Continuum mechanics of electromagnetic solids. North-Holland, Amsterdam

Oliveira DA, Worswick MJ (2003) Electromagnetic forming of aluminium alloy sheet. J de Phys IV 110:293–298

Oliveira DA, Worswick MJ, Finn M, Newman D (2005) Electromagnetic forming of aluminum alloy sheet: free-form and cavity fill experiments and model. J Mater Process Technol 170:350–362

Park Y, Kim H, Oh S (2004) Design and strength evaluation of structural joint made by electro-magnetic forming (EMF). In: Materials processing and design: modeling, simulation and applications—NUMIFORM 2004—Proceedings of the 8th international conference on numerical methods in industrial forming processes. American Institute of Physics

Reese S, Svendsen B, Stiemer M, Unger J, Schwarze M, Blum H (2005) On a new finite element technology for electromagnetic metal forming processes. Arch Appl Mech 74:834–845

Rieben R, Wallin B, White D (2006) Arbitrary lagrangian eulerian electromechanics in 3D. In: Proceedings from progress in electromagnetics research symposium, Cambridge pp 265–269

Seth M, Daehn GS (2005) Effect of aspect ratio on high velocity formability of aluminum alloy. In: Bieler TR, Carsley JE, Fraser HL, Sears JW, Smugeresky JE (eds) Materials processing and manufacturing division sixth global innovations proceedings. Trends in materials and manufacturing technologies for transportation industries and powder metallurgy research and development in the transportation industry, TMS pp 59–64

Seth M, Vohnout VJ, Daehn GS (2005) Formability of steel sheet in high velocity impact. J Mater Process Technol 168:390–400

Stiemer S, Unger J, Svendsen B, Blum H (2006) Algorithmic formulation and numerical implementation of coupled electromagnetic-inelastic continuum models for electromagnetic metal forming. Int J Numer Methods Eng 68: 1301–1328

Stiemer S, Unger J, Blum H, Svendsen B (2007) ALE-based 3D FE simulation of electromagnetic forming. Proc Appl Math Mech 6:459–460

Strand OT, Berzins LV, Goosman DR, Kuhlow WW, Sargis PD, Whitworth TL (2005) Velocimetry using heterodyne techniques. In: Paisley DL, Kleinfelder S, Snyder DR, Thompson BJ (eds) Proceedings of the SPIE: 26th international congress on high-speed photography and photonics, SPIE. Alexandria, p 593

Svendsen B, Chanda T (2005) Continuum thermodynamic formulation of models for electromagnetic thermoinelastic solids with application in electromagnetic metal forming. Continuum Mech Thermodyn 17:1–16

Thomas JD, Seth M, Daehn GS, Bradley JR, Triantafyllidis N (2007) Forming limits for electromagnetically expanded aluminum alloy tubes: theory and experiment. Acta Mater 55:2863–2873

Thomas JD, Triantafyllidis N (2007) Theory of necking localization in unconstrained electromagnetic expansion of thin sheets. Int J Solids Struct 44:6744–6767

Thomas JD, Triantafyllidis N (2009) On electromagnetic forming processes in finitely strained solids: theory and examples. J Mech Phys Solids 57(8):1391–1416

Trimarco C (2007) Material electromagnetic fields and material forces. Arch Appl Mech 77(2–3):177–184

Trimarco C, Maugin GA (2001) Material mechanics of electromagnetic solids. In: Configurational mechanics of materials. CISM courses and lectures, no. 427, Springer, Wien, pp 129–171

Unger J, Stiemer M, Svendsen B, Blum H (2006) Multifield modeling of electromagnetic metal forming processes. J Mater Process Technol 177:270–273

Unger J, Stiemer M, Schwarze M, Svendsen B, Blum H, Reese S (2008) Strategies for 3d simulation of electromagnetic forming processes. J Mater Process Technol 199: 341–362

Vural M, Rittel D, Ravichandran G (2004) High strain rate behavior of metal alloys at large strains. GALCIT Report, Graduate Aeronautical Laboratories, The California Institute of Technology, Pasadena

Yadav S, Chichili D, Ramesh K (1995) The mechanical response of a 6061-T6 Al/Al2O3 metal matrix composite at high rates of deformation. Acta Metall et Mater 43:4453–4464

Yadav S, Repetto EA, Ravichandran G, Ortiz M (2001) A computational study of the influence of thermal softening on ballistic penetration in metals. Int J Impact Eng 25(8):787–803

Zhang H, Ravi-Chandar K (2006) On the dynamics of necking and fragmentation—I. Real-time and post-mortem observations in Al 6061-O. Int J Fract 142:183–217

Zhang H, Ravi-Chandar K (2008) On the dynamics of necking and fragmentation—II. Effect of material properties, geometrical constraints and absolute size. Int J Fract 150:3–36

Zhang H, Liechti KM, Ravi-Chandar K (2008) On the dynamics of necking and fragmentation—III. Effect of cladding with a polymer. Int J Fract 155(2):101–118